Postprint of: Macewicz Ł., Pyrchla K., Bogdanowicz R., Sumanasekera G., Jasinski J. B., Chemical Vapor Transport Route toward Black Phosphorus Nanobelts and Nanoribbons, Journal of Physical Chemistry Letters, Vol. 12, iss. 34 (2021), pp. 8347-8354

Chemical Vapor Transport Route Towards Black Phosphorus Nanobelts and Nanoribbons

Lukasz Macewicz[1,3], *Krzysztof Pyrchla*[1], *Robert Bogdanowicz*[1*], *Gamini Sumanasekera*[2] *and Jacek B. Jasinski*[3*]

[1] Gdańsk University of Technology, Faculty of Electronics, Telecommunications and Informatics, Narutowicza str. 11/12, 80-233 Gdańsk, Poland

[2] Department of Physics, University of Louisville, Louisville, Kentucky 40292, United States

[3] Institute for Advanced Materials and Renewable Energy, University of Louisville, Louisville, KY, 40292

KEYWORDS: Nanoribbons, Nanobelts, Phosphorene, Chemical Vapor Transport, LCAO method

ABSTRACT

Chemical Vapor Transport (CVT) method is widely used for bulk black phosphorus (BP) fabrication. In this paper, we demonstrate that CVT provides a route for the fabrication of BP nanoribbons and nanobelts. This method consists of a two-step procedure, including initial BP column growth using the CVT technique, followed by ultrasonic treatment and centrifugation. The obtained nanostructures preserve BP column dimensions, forming ultra-long ribbon-like structures with the length to the width aspect ratio of up to 500. Computational modeling of the growth mechanism of a BP flake is also presented in support of the observed columnar growth. Calculation of the average energy of the molecule in the asymmetric flakes shows that the growth of the structure in the zigzag direction is more energetically favorable than in the armchair direction.

1. INTRODUCTION

The family of two-dimensional (2D) materials has been expanding rapidly ever since the fabrication of the first single atomic layer, opening doors for new applications in nearly every aspect of life and physical sciences[1–5]. 2D materials like MoS_2, graphene or silicene exhibit extraordinary chemical[6,7], mechanical [8–10] and optical properties[11–13] in comparison to their three-dimensional (3D) counterparts, with new functionalities and applications including sensors[14,15], electronics[16], optoelectronics[17] and photovoltaics[18,19]. Our ever-expanding knowledge of possible applications of thin layered structures results in rediscovering van der Waals (vdW) layered materials like black phosphorus (BP). Exploration of facile, fast and inexpensive synthesis methods of nanoscale materials is essential for the discovery of novel and everyday technologies.

BP, being the most stable of all phosphorus allotropes, has drawn a lot of attention due to its extraordinary properties, which has resulted in many studies covering its synthesis and modification possibilities[8–13]. The most common method of synthesizing 2D materials is a process called exfoliation, which is a top-down approach of separating single atomic layers from a bulk precursor. Layered materials exhibit strong in-plane chemical bonds but rather weak out-of-plane vdW bonds, enabling the exfoliation process[14].

Phosphorene, a single layer of BP, has a puckered honeycomb structure[15]. One of its most important properties is a tunable bandgap ranging from 0.3 eV to 2.0 eV with thickness scaling[16]. Despite the fact that there are many semiconducting 2D materials, those with the bandgap in the range from 0.3 eV to 1.5 eV are noticeably missing[17]. These particular bandgap values are especially important for optoelectronic applications, such as solar energy harvesting[18], photocatalysis[19,20], photodetection[21] etc., because they correspond to a spectral range of visible and infrared radiation. Additionally, phosphorene has direction dependent electronic[22] and optical[23] properties arising from highly anisotropic puckered honeycomb structures. This highly anisotropic behavior, along with strong energy dispersion[24] and high carrier mobility[25] enables a wide range

of possible applications, from electronic[26–29], spintronic[30] and optoelectronic[31] devices, to sensors[32], thermoelectrics[33] and batteries[34].

While 2D materials exhibit a quantum confinement in one direction, downsizing in other directions can lead to one-dimensional (1D) and zero-dimensional (0D) structures. For example, converting 2D graphene into graphene nanoribbons (i.e., 1D objects), graphene quantum dots (i.e., 0D objects) with enhanced quantum confinement and edge effects gives rise to the new properties enabling new phenomena and applications in disciplines such as physics, biology, materials, chemistry, etc.[35,36] Similarly, reducing transition metal phosphide size to 0D nanocrystals results in significant new properties, directly enhancing catalytic performance of these structures, including enormous surface-to-volume ratio, prominent edges, and a large number of active sites[37]. Further, in the case of BP, reducing it to a size of less than 20 nm will result in 0D quantum dots formation, which apart from bulk phosphorus specificity will be have high absorption coefficient and facile hybridization with various materials[38–40].

Recent theoretical studies predict that BP nanoribbons could surpass optical and mechanical properties of phosphorene[41,42]. Additionally, properties such as carrier mobility and electronic structure can be controlled by changing the nanoribbon dimensions[43,44]. The production of nanoribbons for many materials usually remains a challenge. Despite many examples of fabrication methods of graphene nanoribbons, only few are applicable[45] to other 2D materials. In particular, for BP, most techniques are based on top-down processes, including electron-beam lithography[46,47], which is restricted to nanoribbons fabrication of well-defined dimensions and electronic properties similar to those of bulk BP. The challenge of this approach is also the scalability. Only recently, a scalable top-down method based on the combination of Li-intercalation and mechanical exfoliation has been demonstrated to produce phosphorus nanoribbons[48]. However, while this intercalation-based method is promising, the procedure is time-consuming and includes several steps, making its application challenging at a large scale.

In this paper, we demonstrate that Chemical Vapor Transport (CVT), a widely used method for the synthesis of BP, offers a route for the fabrication of BP nanoribbons and nanobelts. Our method consists of two-step procedure, which includes BP columns growth using chemical vapor transport techniques, followed by ultrasonic treatment and centrifugation. In order to establish the structural properties of fabricated structures, Raman spectroscopy was performed. Surface morphology was obtained using optical and scanning electron microscopy (SEM). The crystal structure and chemical composition was measured with (scanning) transmission electron microscopy (S)TEM and energy-dispersive X-ray spectroscopy (EDS), respectively. The theoretical effort was carried out to check which structure configuration may be most energetically favorable. The adsorption energy of common impurities on the edge of phosphorene nanoflakes were calculated. The average energy of the flake versus its size was additionally calculated. Most of the reported theoretical studies have focused on a few subjects, including phosphorene interaction with metallic dopants[49,50] or biomolecules[51,52] and electronic structure of various nanostructures of phosphorene[53,54]. In this study, we have looked into the molecular dynamics simulations of phosphorene asymmetric flakes in order to establish if the zigzag direction could be energetically favorable compared to the armchair direction. These calculations could give us the explanation of BP nanocolumns formation mechanism during the CVT synthesis.

2. EXPERIMENTAL

2.1. Growth of BP columns through chemical vapor transport

BP columns were fabricated by the reaction of red phosphorus (250mg), Sn (10 mg) and SnI_4 (5 mg) in an evacuated quartz ampule. The ampules were customized to have a restriction in the middle, enabling an easy sealing process. The reagents were placed at the far end of the ampule while silicon substrates were located just after the restriction. Using a diffusion pump system, the tube was evacuated down to 10^{-5} Torr. Afterwards the ampule was sealed with an oxy-acetylene torch.

The sealed ampule was placed horizontally in a tube furnace with two independent heating zones (Fig. 1a). The two-step heating synthesis process involved temperature-programmed reactions, constant temperature heating, and slow cooling treatment, as shown in figure 1b. In order to ensure the CVT process, a temperature gradient of 50 ^{O}C was maintained with the silicon substrates kept in lower temperature and the end of the vial containing the precursor material in the hotter zone (Fig. 1a). After reaching room temperature, a homogeneous layer of column-like BP was found to be formed on the substrate surface. Since BP is not stable in ambient conditions, the fabricated structures were stored in an argon glove box to prevent any degradation.

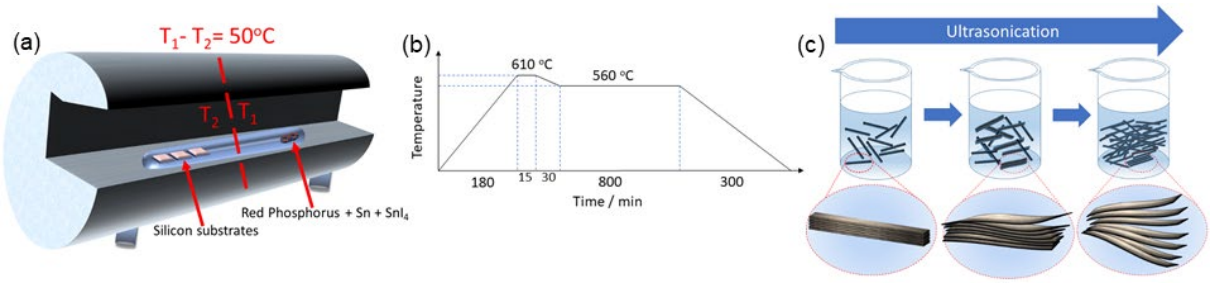

Figure 1. (a) A schematic of a quartz ampule with silicon substrate and precursors placed inside the tube furnace (a). (b) A temperature profile of the used two-step heating synthesis process, and (c) a schematic process of nanoribbon formation.

2.2. BP nanoribbon fabrication

In order to obtain BP nanoribbons (Fig. 1c), silicon substrates with BP columns were placed in a glass beaker with 5 ml of DMF and subject to ultrasonic treatment for 10 minutes. Afterwards, 1 ml of DMF with BP particles was separated and subjected to the centrifugation (2000 rpm for 5 minutes). The final step was to drop-cast the solution onto silicon substrate for further measurements.

2.3. Characterization

Raman spectroscopy was performed on a Renishaw in Via Raman Microscope, equipped with a Nd:YAG laser with an emission line of 532 nm. Scanning electron microscopy (SEM) imaging

was recorded on an FEI Nova 600 microscope. Standard transmission electron microscopy (TEM) images were recorded using a FEI Tecnai F20. Various types of TEM-based measurements, including high resolution (HR) TEM, selected area electron diffraction (SAED) and energy dispersive X-ray spectroscopy (EDX), were used to study the crystalline structure of fabricated structures. Atomic force microscopy (AFM) was performed on a Asylum MFP-3D-Bio AFM.

2.4. Computational modelling

For the simulation, the ab-initio DFT method was applied. The Linear Combination of Atomic Orbitals[55] (LCAO) was used both for force estimation during structure optimization and in total energy calculations. The series of structures models with different sizes were generated using the Atomistix ToolKit Quantumwise (ATK, Synopsys, USA).

3. RESULTS AND DISCUSSION

3.1. Surface morphology and structural properties

BP, as many layered materials, is known to form micro and sub-micro column structures. However, in most cases the column growth is based either on glancing angle deposition[56], vapor deposition on topographic substrates[57] or selective etching through masks[47]. Fig 2d,e and f presents a single BP column fabricated by chemical vapor deposition on silicon substrates with a majority of column dimensions being up to 1.5 μm in width and more than 500 μm in length. Subsequent treatment with ultrasonication and centrifugation results in the formation of BP nanoribbons presented in figure 3a and b. Applying low-speed ultrasonication allows the fabricated columns to be exfoliated and the resulting nanoribbons preserve their original dimensions forming ultra-long nanoribbon structures. Figure 3b presents a magnified single BP nanoribbon. It can be noticed that a few breaks occur along the structure, which might be caused due to the exposure of nanoribbons to oxygen, leading to deformation[58]. Watts et al[48] have reported BP nanoribbon fabrication with

their length to width ratio up to 80. Using our approach, we can obtain similar structures with an aspect ratio up to 500.

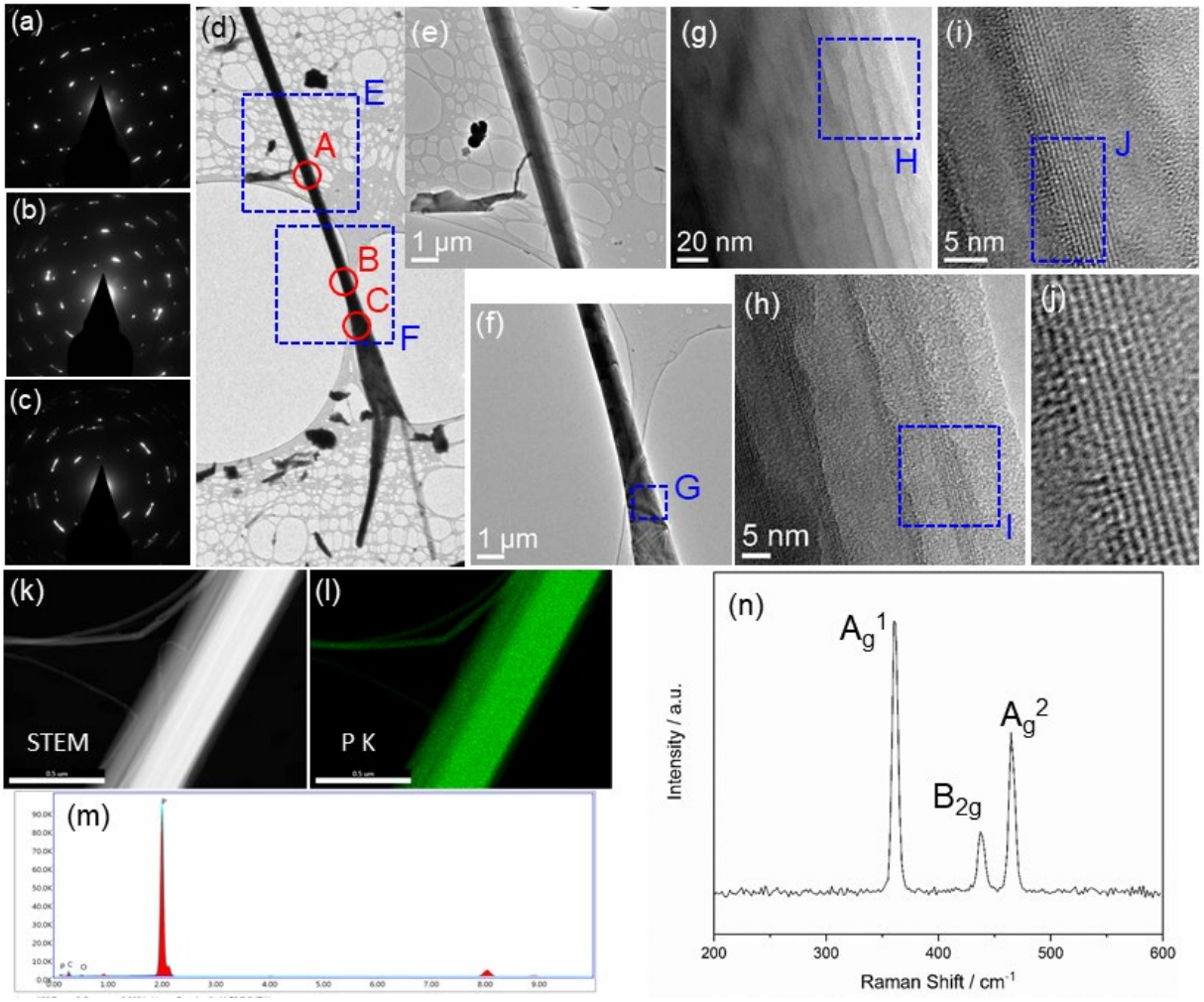

Figure 2. BP columns characterization: (a-c) SEAD patterns from the 3 areas along the single BP column shown in (d-h) TEM and (i-j) HRTEM images. (k) STEM image and (l) phosphorous map of a single BP column. (m) EDS spectrum from the same region, (n) Raman spectrum of a single BP column.

In order to further investigate the fabricated structures surface morphology AFM images were collected (Fig. 3c-d). The nanoribbons were found to form elongated structures resembling BP columns even when they were not fully exfoliated. Considering phosphorene monolayer to have a thickness of 0.85-0.9 nm[59,60], the fabricated nanoribbons studied with AFM (Fig. 3c-d) have a thickness up to 10 nm, which corresponds to approximately 11 layers[61]. Moreover, subjecting this

structure to the subsequent ultrasonic liquid-phase exfoliation process could result in the exfoliation of a single ribbon, similarly to experiments reported for BP crystals[62–64] by being the source of nanosheets with centrifugation-controlled size.

According to theoretical studies, there are six Raman active modes of the twelve possible lattice vibrational modes in black phosphorus. However, only three vibrational modes can be detected with the incident laser being perpendicular to the phosphorus plane. Figure 2n presents Raman spectra recorded for black phosphorus fabricated on silicon substrate. Raman data was collected from a single column and the obtained spectra show three Raman peaks at 361.2 cm^{-1}, 437.8 cm^{-1} and 465.1 cm^{-1} corresponding to the A_g^1, B_{2g} and A_g^2 modes respectively. All visible peaks are slightly shifted towards lower wavenumbers in comparison to the literature, which strongly indicate the black phosphorus columns may consist of even few layers[59,65].

3.2. Crystal structure

Transmission electron microscopy was used to further probe the fabricated BP columns and nanoribbons. SEAD patterns (Fig. 2a-c) obtained from 3 different areas (A, B and C) of a single BP column (Fig. 2d) shine light on the mechanism of nanoribbon formation. From these patterns, it can be noticed that while in area A (Fig. 2a) the diffraction spots are sharp and almost single-crystalline, SEAD patterns for areas B and C (Fig. 2b,c) show elongated arcs instead of sharp spots, which indicates a gradual and continuous change of crystal orientation. This effect is stronger in area C which is further away from "undistorted" area A. Concerning the mechanism, this effect occurs due to the separation and continuously propagating small twist between subsequent sheets of BP. The observed arcing of diffraction spots is a strong indication of the exfoliation process starting within the nanoribbon. This is directly confirmed by TEM images acquired from this nanoribbon (Fig. 2d-j). In particular, a clear separation of the individual layers and the beginning of exfoliation process can be seen in images taken from the area C (Fig. 2f-j).

TEM images (Fig. 3f-g) confirm the width of BP nanoribbons to be around 1 μm. It can also be seen that the obtained structures consist of few layers and have many folds, which may indicate high flexibility of the material. The crystallinity of the BP nanoribbons was confirmed by SAED patterns (Fig. 3i). Furthermore, SEAD patterns were used to measure the lattice parameters a = 3.49 Å and c = 4.58 Å. The lattice parameters obtained from d-spacing of lattice fringes visible in HRTEM images (such as in Fig. 3j) agree, within experimental errors of few %, with values obtained from SAED patterns. The obtained c/a ratio is equal to 1.312, which agrees with the accuracy of 0.5% with the expected ratio of c/a = 1.319.

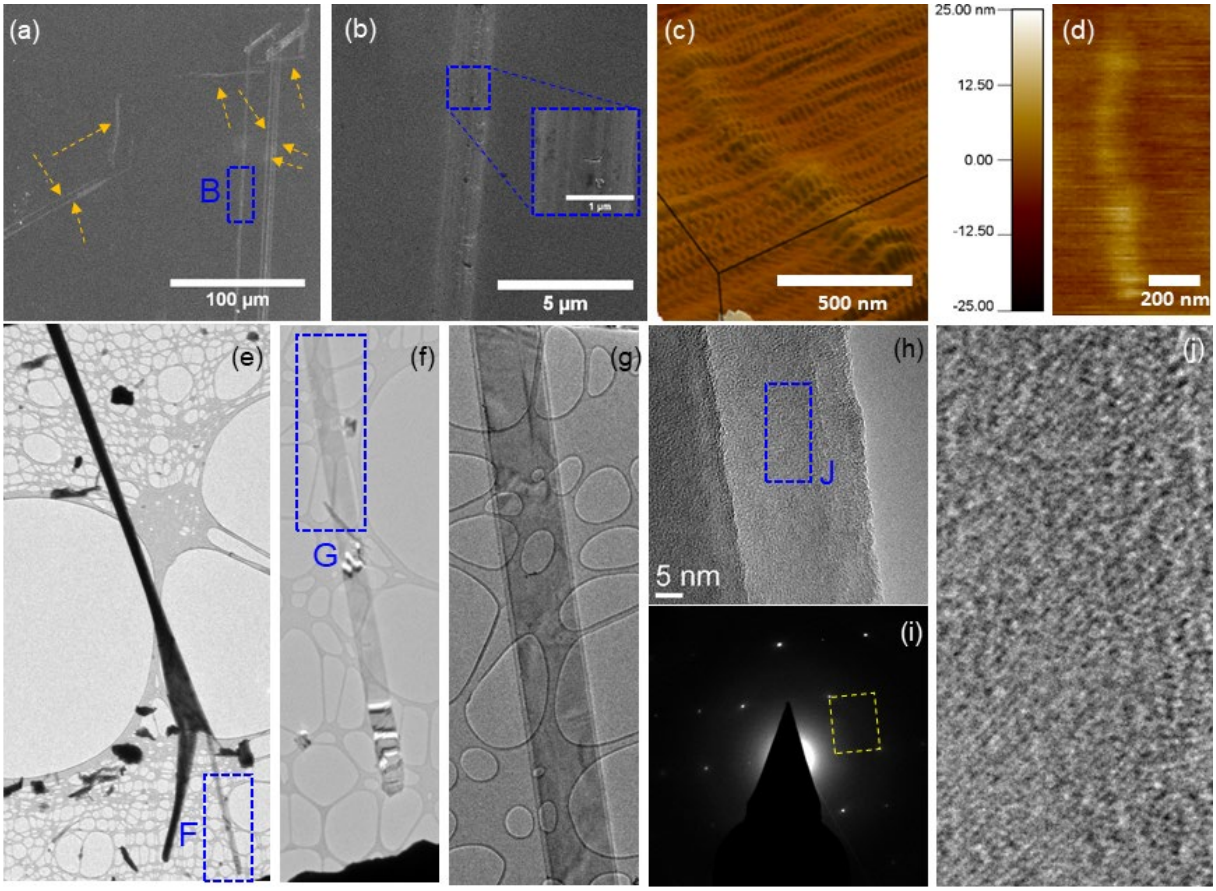

Figure 3. Characterization of few-layer black phosphorus nanoribbons: (a-b) SEM images of fabricated BP nanoribbons, (c-d) AFM studies of fabricated structures, (e-h) TEM images of an exfoliated black phosphorus nanoribbon, and (i) SEAD pattern from area shown in HRTEM image in (j).

3.3. Elemental composition

In order to confirm the elemental composition of fabricated structures, a nanoprobe-based STEM-EDX analysis was performed. Figure 2k- m presents respectively a STEM image, phosphorus K-line map, and EDX spectrum of a single BP column. This spectrum (Fig 2m) confirms that the column consists primarily of phosphorous. Small residual peaks of carbon and oxygen detected in the spectrum are related to the surface contamination from the preparation process and transferring the specimen to the microscope. The phosphorous K-line map (Fig. 2l) of this BP column shows very uniform distribution of phosphorous across the entire column. In fact, the contrast of the phosphorous map matches exactly the contrast of the STEM image (Fig. 2k) obtained for this column. These results confirm this fabrication method to be successful and the obtained structures to almost exclusively consist of phosphorus.

3.3. Average flake energy and adsorption energy

In order to better understand the mechanism of BP nanocolumn growth, we conducted DFT calculations of flakes with different aspect ratio, defined by the ratio of unit cells in the a- and c-crystallographic direction, and analyzed the total energy of such model structures. We used the following notation to describe the phosphorene nanoflake size: <number of primitive cells along the zigzag direction> x <number of primitive cells along the armchair direction>. To solve the matrix equations of the LCAO method, self-consistent field (SCF) iterations were performed. During DFT calculation, the exchange-correlation of electrons was included using GGA method witch PBE (Perdew, Burke and Ernzerhof) functionals. The PseudoDojo[66] pseudopotentials with medium basis set were utilized to calculate the electron wave functions. The detailed description of the mentioned basis set can be found in the appendix of Ref [67]. The residual forces in the structure were relaxed using the Broyden-Fletcher-Goldfarb-Shanno (LBFGS) algorithm. The maximal force in the structure after optimization does not exceed 0.05 eV/Ang. For each optimized structure, the average molecule energy was calculated. The average energy can be expressed by equation 1.

$$E_{avr} = \frac{1}{N} E_{total} \quad (1)$$

where, E_{total} is the total energy of the system and the N denotes the number of atoms in the system. The resulting average energy for both symmetric and asymmetric flakes is presented in Figure 4.

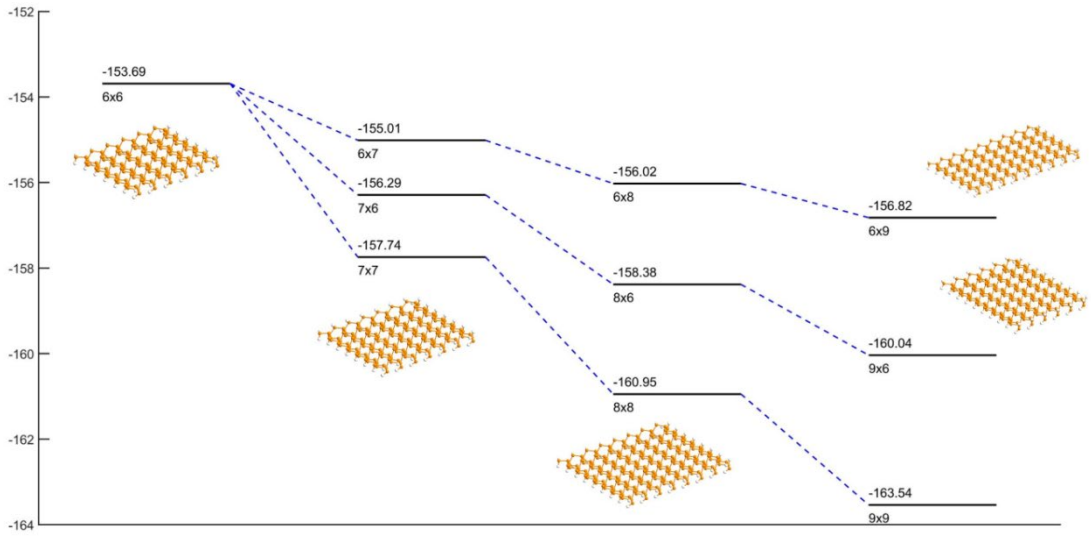

Figure 4. The changes in the average energy of a molecule in respect to different phosphorene flakes sizes.

One of the reasons for the preferred nanoribbon zigzag direction of growth could be the anisotropic thermal conductivity of phosphorene. The molecular dynamics simulations[68] showed much higher thermal conductivity along the zigzag than the one along the armchair direction, providing effectively required energy for CVT-based BP column growth[47]. Such an anisotropy was mainly manifested by acoustic photon dispersion versus specific axial direction. Similar observations were reported for monolayer WS_2[69], where temperature flux dependent behavior was postulated towards isotropic crystal formation by means of Monte Carlo simulations. Chen et al. reported temperature-dependent tuning of growth mode of $MoSe_2$ nanoribbons, thanks to the non-equilibrium conditions inducing specific shape transformations[70–72]. Moreover, Zhang et al.[73] reported both planar and columnar zigzag ribbons to be more thermodynamically stable and energetically favored over armchair nanoribbons dominating nanostructures synthesized in the carbon nanotubes (CNT)

templates. These findings were supported by ab-initio DFT calculations and TEM observations. Yu et al.[74] postulated that the utilization of Pb in CVT facilitates adsorption of P_4 clusters along the zigzag direction thanks to the strong vdW interactions.

A recent study reporting nanobelt formation[75] revealed that metastable interstitial oxygen defects in phosphorene allows for the formation of a P–O–P bridge structure leading to a clean-cut edge along the zigzag direction. This effect is not observed along the armchair direction, indicating that the zigzag-oriented ribbons are energetically favorable. Next, DFT studies[76] exhibited that zigzag edges are more resistant to the abstraction of single atoms than armchair ones, where energy drops below zero reference level. Experimentally, the armchair edges diminish faster under electron-beam treatment leaving the zigzag edge slightly longer[76]. The scissoring method of macroscopic BP crystals[48] also results in zigzag-edge-aligned NRs production like fabricated here for the first time with discrete high-quality and large quantity PNRs. The alkali metal directional diffusion and intercalation along the zigzag direction was claimed to be essential for PNR process formation, whereas strain between differently intercalated regions jointly with high electron densities causes a break of longer and lower energy P-P bonds[77]. However, there are still uncertainties concerning the exact growth mechanism of nanoribbons and related highly anisotropic nanostructures. In a recent review on vapor phase growth of nanowires, Gu̇niat et al.[78] stated that independently on the initial mechanism of growth it is not clear why polytypism exists in this kind of synthesis.

4. CONCLUSIONS

In conclusion, we present a novel CVT-based approach for the fabrication of BP nanoribbons and nanobelts fabrication. The ribbon-like structures obtained through this approach are monocrystalline and consist almost exclusively of BP as confirmed by Raman and TEM measurements. Their dimensions can vary depending on the conditions of the CVT method used for BP columns growth and the post-growth ultrasonication treatment. The obtained nanoribbons/nanobelts preserve BP column dimensions. The forming of ultra-long ribbon-like

structures with the length-to-width aspect ratio of up to 500 was demonstrated. The fabrication process allows for a high degree of control, which could be used for production of BP nanoribbons and nanobelts with well controlled dimensions suitable for specific applications. DFT-based calculations of the average energy of the molecule in the asymmetric BP flakes shows that growth of the structure in the zigzag direction is more energetically favorable than that in the armchair direction. The calculations show a significantly asymmetry of adatoms adsorption energy.

AUTHOR INFORMATION

Corresponding Authors

* Jacek B. Jasinski (jacek.jasinski@louisville.edu)

* Robert Bogdanowicz (rbogdan@eti.pg.edu.pl)

Author Contributions

The manuscript was written through contributions of all authors. All authors have given approval to the final version of the manuscript.

ACKNOWLEDGEMENT

Funding Sources

This work was partially financed by European Social Fund from project InterPhD2 (POWR.03.02.00-00-I002/16). The authors would like to acknowledge the support from the Poland National Science Centre through the Research Grant No. 2016/22/E/ST7/00102 and the U.S. Department of Energy, Office of Science, Basic Energy Sciences, under Award # DE-SC0019348.

REFERENCES

(1) Zhang, X.; Hou, L.; Ciesielski, A.; Samorì, P. 2D Materials Beyond Graphene for High-Performance Energy Storage Applications. *Advanced Energy Materials* **2016**, *6* (23), 1600671. https://doi.org/10.1002/aenm.201600671.

(2) Huo, C.; Yan, Z.; Song, X.; Zeng, H. 2D Materials via Liquid Exfoliation: A Review on Fabrication and Applications. *Science Bulletin* **2015**, *60* (23), 1994–2008. https://doi.org/10.1007/s11434-015-0936-3.

(3) Lin, Z.; McCreary, A.; Briggs, N.; Subramanian, S.; Zhang, K.; Sun, Y.; Li, X.; Borys, N. J.; Yuan, H.; Fullerton-Shirey, S. K.; Chernikov, A.; Zhao, H.; McDonnell, S.; Lindenberg, A. M.; Xiao, K.; LeRoy, B. J.; Drndić, M.; Hwang, J. C. M.; Park, J.; Chhowalla, M.; Schaak, R. E.; Javey, A.; Hersam, M. C.; Robinson, J.; Terrones, M. 2D Materials Advances: From Large Scale Synthesis and Controlled Heterostructures to Improved Characterization Techniques, Defects and Applications. *2D Mater.* **2016**, *3* (4), 042001. https://doi.org/10.1088/2053-1583/3/4/042001.

(4) Luo, B.; Liu, G.; Wang, L. Recent Advances in 2D Materials for Photocatalysis. *Nanoscale* **2016**, *8* (13), 6904–6920. https://doi.org/10.1039/C6NR00546B.

(5) Vogt, P. Silicene, Germanene and Other Group IV 2D Materials. *Beilstein Journal of Nanotechnology* **2018**, *9*, 2665–2667. https://doi.org/10.3762/bjnano.9.248.

(6) Chen, W.; Santos, E. J. G.; Zhu, W.; Kaxiras, E.; Zhang, Z. Tuning the Electronic and Chemical Properties of Monolayer MoS_2 Adsorbed on Transition Metal Substrates. *Nano Lett.* **2013**, *13* (2), 509–514. https://doi.org/10.1021/nl303909f.

(7) Ma, D.; Ju, W.; Li, T.; Zhang, X.; He, C.; Ma, B.; Tang, Y.; Lu, Z.; Yang, Z. Modulating Electronic, Magnetic and Chemical Properties of MoS2 Monolayer Sheets by Substitutional Doping with Transition Metals. *Applied Surface Science* **2016**, *364*, 181–189. https://doi.org/10.1016/j.apsusc.2015.12.142.

(8) Liu, H.; Du, Y.; Deng, Y.; Ye, P. D. Semiconducting Black Phosphorus: Synthesis, Transport Properties and Electronic Applications. *Chem. Soc. Rev.* **2015**, *44* (9), 2732–2743. https://doi.org/10.1039/C4CS00257A.

(9) Yi, Y.; Yu, X.-F.; Zhou, W.; Wang, J.; Chu, P. K. Two-Dimensional Black Phosphorus: Synthesis, Modification, Properties, and Applications. *Materials Science and Engineering: R: Reports* **2017**, *120*, 1–33. https://doi.org/10.1016/j.mser.2017.08.001.

(10) Eswaraiah, V.; Zeng, Q.; Long, Y.; Liu, Z. Black Phosphorus Nanosheets: Synthesis, Characterization and Applications. *Small* **2016**, *12* (26), 3480–3502. https://doi.org/10.1002/smll.201600032.

(11) Xu, Y.; Wang, Z.; Guo, Z.; Huang, H.; Xiao, Q.; Zhang, H.; Yu, X.-F. Solvothermal Synthesis and Ultrafast Photonics of Black Phosphorus Quantum Dots. *Advanced Optical Materials* **2016**, *4* (8), 1223–1229. https://doi.org/10.1002/adom.201600214.

(12) Batmunkh, M.; Bat-Erdene, M.; Shapter, J. G. Black Phosphorus: Synthesis and Application for Solar Cells. *Advanced Energy Materials* **2018**, *8* (5), 1701832. https://doi.org/10.1002/aenm.201701832.

(13) Ling, X.; Wang, H.; Huang, S.; Xia, F.; Dresselhaus, M. S. The Renaissance of Black Phosphorus. *Proc Natl Acad Sci USA* **2015**, *112* (15), 4523–4530. https://doi.org/10.1073/pnas.1416581112.

(14) Cai, M.; Thorpe, D.; Adamson, D. H.; Schniepp, H. C. Methods of Graphite Exfoliation. *J. Mater. Chem.* **2012**, *22* (48), 24992–25002. https://doi.org/10.1039/C2JM34517J.

(15) Hultgren, R.; Gingrich, N. S.; Warren, B. E. The Atomic Distribution in Red and Black Phosphorus and the Crystal Structure of Black Phosphorus. *J. Chem. Phys.* **1935**, *3* (6), 351–355. https://doi.org/10.1063/1.1749671.
(16) Peng, X.; Wei, Q.; Copple, A. Strain-Engineered Direct-Indirect Band Gap Transition and Its Mechanism in Two-Dimensional Phosphorene. *Phys. Rev. B* **2014**, *90* (8), 085402. https://doi.org/10.1103/PhysRevB.90.085402.
(17) Gupta, A.; Sakthivel, T.; Seal, S. Recent Development in 2D Materials beyond Graphene. *Progress in Materials Science* **2015**, *73*, 44–126. https://doi.org/10.1016/j.pmatsci.2015.02.002.
(18) Mishra, A.; Bäuerle, P. Small Molecule Organic Semiconductors on the Move: Promises for Future Solar Energy Technology. *Angewandte Chemie International Edition* **2012**, *51* (9), 2020–2067. https://doi.org/10.1002/anie.201102326.
(19) Mills, A.; Le Hunte, S. An Overview of Semiconductor Photocatalysis. *Journal of Photochemistry and Photobiology A: Chemistry* **1997**, *108* (1), 1–35. https://doi.org/10.1016/S1010-6030(97)00118-4.
(20) Xiang, Q.; Yu, J.; Jaroniec, M. Graphene-Based Semiconductor Photocatalysts. *Chem. Soc. Rev.* **2012**, *41* (2), 782–796. https://doi.org/10.1039/C1CS15172J.
(21) Fan, P.; Chettiar, U. K.; Cao, L.; Afshinmanesh, F.; Engheta, N.; Brongersma, M. L. An Invisible Metal–Semiconductor Photodetector. *Nature Photon* **2012**, *6* (6), 380–385. https://doi.org/10.1038/nphoton.2012.108.
(22) Fei, R.; Yang, L. Strain-Engineering the Anisotropic Electrical Conductance of Few-Layer Black Phosphorus. *Nano Lett.* **2014**, *14* (5), 2884–2889. https://doi.org/10.1021/nl500935z.
(23) Tran, V.; Soklaski, R.; Liang, Y.; Yang, L. Layer-Controlled Band Gap and Anisotropic Excitons in Few-Layer Black Phosphorus. *Phys. Rev. B* **2014**, *89* (23), 235319. https://doi.org/10.1103/PhysRevB.89.235319.
(24) Jain, A.; McGaughey, A. J. H. Strongly Anisotropic In-Plane Thermal Transport in Single-Layer Black Phosphorene. *Scientific Reports* **2015**, *5*, 8501. https://doi.org/10.1038/srep08501.
(25) Li, P.; Appelbaum, I. Electrons and Holes in Phosphorene. *Phys. Rev. B* **2014**, *90* (11), 115439. https://doi.org/10.1103/PhysRevB.90.115439.
(26) Li, L.; Yu, Y.; Ye, G. J.; Ge, Q.; Ou, X.; Wu, H.; Feng, D.; Chen, X. H.; Zhang, Y. Black Phosphorus Field-Effect Transistors. *Nature Nanotech* **2014**, *9* (5), 372–377. https://doi.org/10.1038/nnano.2014.35.
(27) Das, S.; Zhang, W.; Demarteau, M.; Hoffmann, A.; Dubey, M.; Roelofs, A. Tunable Transport Gap in Phosphorene. *Nano Lett.* **2014**, *14* (10), 5733–5739. https://doi.org/10.1021/nl5025535.
(28) Das, S.; Demarteau, M.; Roelofs, A. Erratum: Ambipolar Phosphorene Field Effect Transistor (ACS Nano (2014) 8:11 (11730-11738) DOI: 10.1021/Nn505868h). *ACS nano* **2016**, *10* (2). https://doi.org/10.1021/acsnano.6b00680.
(29) Sebastian, A.; Pannone, A.; Subbulakshmi Radhakrishnan, S.; Das, S. Gaussian Synapses for Probabilistic Neural Networks. *Nat Commun* **2019**, *10* (1), 4199. https://doi.org/10.1038/s41467-019-12035-6.
(30) Babar, R.; Kabir, M. Transition Metal and Vacancy Defect Complexes in Phosphorene: A Spintronic Perspective. *J. Phys. Chem. C* **2016**, *120* (27), 14991–15000. https://doi.org/10.1021/acs.jpcc.6b05069.
(31) Xia, F.; Wang, H.; Jia, Y. Rediscovering Black Phosphorus as an Anisotropic Layered Material for Optoelectronics and Electronics. *Nat Commun* **2014**, *5* (1), 1–6. https://doi.org/10.1038/ncomms5458.
(32) Cui, S.; Pu, H.; Wells, S. A.; Wen, Z.; Mao, S.; Chang, J.; Hersam, M. C.; Chen, J. Ultrahigh Sensitivity and Layer-Dependent Sensing Performance of Phosphorene-Based Gas Sensors. *Nat Commun* **2015**, *6* (1), 1–9. https://doi.org/10.1038/ncomms9632.

(33) Fei, R.; Faghaninia, A.; Soklaski, R.; Yan, J.-A.; Lo, C.; Yang, L. Enhanced Thermoelectric Efficiency via Orthogonal Electrical and Thermal Conductances in Phosphorene. *Nano Lett.* **2014**, *14* (11), 6393–6399. https://doi.org/10.1021/nl502865s.
(34) Sun, J.; Lee, H.-W.; Pasta, M.; Yuan, H.; Zheng, G.; Sun, Y.; Li, Y.; Cui, Y. A Phosphorene–Graphene Hybrid Material as a High-Capacity Anode for Sodium-Ion Batteries. *Nature Nanotechnology* **2015**, *10* (11), 980–985. https://doi.org/10.1038/nnano.2015.194.
(35) Haque, E.; Kim, J.; Malgras, V.; Reddy, K. R.; Ward, A. C.; You, J.; Bando, Y.; Hossain, M. S. A.; Yamauchi, Y. Recent Advances in Graphene Quantum Dots: Synthesis, Properties, and Applications. *Small Methods* **2018**, *2* (10), 1800050. https://doi.org/10.1002/smtd.201800050.
(36) Yan, Y.; Gong, J.; Chen, J.; Zeng, Z.; Huang, W.; Pu, K.; Liu, J.; Chen, P. Recent Advances on Graphene Quantum Dots: From Chemistry and Physics to Applications. *Advanced Materials* **2019**, *31* (21), 1808283. https://doi.org/10.1002/adma.201808283.
(37) Luo, Z.-Z.; Zhang, Y.; Zhang, C.; Tan, H. T.; Li, Z.; Abutaha, A.; Wu, X.-L.; Xiong, Q.; Khor, K. A.; Hippalgaonkar, K.; Xu, J.; Hng, H. H.; Yan, Q. Multifunctional 0D–2D Ni2P Nanocrystals–Black Phosphorus Heterostructure. *Advanced Energy Materials* **2017**, *7* (2), 1601285. https://doi.org/10.1002/aenm.201601285.
(38) Sun, Z.; Xie, H.; Tang, S.; Yu, X.-F.; Guo, Z.; Shao, J.; Zhang, H.; Huang, H.; Wang, H.; Chu, P. K. Ultrasmall Black Phosphorus Quantum Dots: Synthesis and Use as Photothermal Agents. *Angewandte Chemie International Edition* **2015**, *54* (39), 11526–11530. https://doi.org/10.1002/anie.201506154.
(39) Zhu, C.; Xu, F.; Zhang, L.; Li, M.; Chen, J.; Xu, S.; Huang, G.; Chen, W.; Sun, L. Ultrafast Preparation of Black Phosphorus Quantum Dots for Efficient Humidity Sensing. *Chemistry – A European Journal* **2016**, *22* (22), 7357–7362. https://doi.org/10.1002/chem.201600719.
(40) Zhang, X.; Xie, H.; Liu, Z.; Tan, C.; Luo, Z.; Li, H.; Lin, J.; Sun, L.; Chen, W.; Xu, Z.; Xie, L.; Huang, W.; Zhang, H. Black Phosphorus Quantum Dots. *Angewandte Chemie International Edition* **2015**, *54* (12), 3653–3657. https://doi.org/10.1002/anie.201409400.
(41) Xie, F.; Fan, Z.-Q.; Zhang, X.-J.; Liu, J.-P.; Wang, H.-Y.; Liu, K.; Yu, J.-H.; Long, M.-Q. Tuning of the Electronic and Transport Properties of Phosphorene Nanoribbons by Edge Types and Edge Defects. *Organic Electronics* **2017**, *42*, 21–27. https://doi.org/10.1016/j.orgel.2016.12.020.
(42) Kumawat, R. L.; Pathak, B. Phosphorene Nanoribbon Based Nano-Electrodes for Explosives Detection: A DFT Study. 24.
(43) Debu, D. T.; Bauman, S. J.; French, D.; Churchill, H. O. H.; Herzog, J. B. Tuning Infrared Plasmon Resonance of Black Phosphorene Nanoribbon with a Dielectric Interface. *Sci Rep* **2018**, *8* (1), 1–10. https://doi.org/10.1038/s41598-018-21365-2.
(44) Carvalho, A.; Rodin, A. S.; Neto, A. H. C. Phosphorene Nanoribbons. *EPL* **2014**, *108* (4), 47005. https://doi.org/10.1209/0295-5075/108/47005.
(45) Campos-Delgado, J.; Romo-Herrera, J. M.; Jia, X.; Cullen, D. A.; Muramatsu, H.; Kim, Y. A.; Hayashi, T.; Ren, Z.; Smith, D. J.; Okuno, Y.; Ohba, T.; Kanoh, H.; Kaneko, K.; Endo, M.; Terrones, H.; Dresselhaus, M. S.; Terrones, M. Bulk Production of a New Form of Sp2 Carbon: Crystalline Graphene Nanoribbons. *Nano Lett.* **2008**, *8* (9), 2773–2778. https://doi.org/10.1021/nl801316d.
(46) Li, L. L.; Peeters, F. M. Quantum Transport in Defective Phosphorene Nanoribbons: Effects of Atomic Vacancies. *Phys. Rev. B* **2018**, *97* (7), 075414. https://doi.org/10.1103/PhysRevB.97.075414.
(47) Lee, S.; Yang, F.; Suh, J.; Yang, S.; Lee, Y.; Li, G.; Sung Choe, H.; Suslu, A.; Chen, Y.; Ko, C.; Park, J.; Liu, K.; Li, J.; Hippalgaonkar, K.; Urban, J. J.; Tongay, S.; Wu, J. Anisotropic In-Plane Thermal Conductivity of Black Phosphorus Nanoribbons at Temperatures Higher than 100 K. *Nat Commun* **2015**, *6* (1), 8573. https://doi.org/10.1038/ncomms9573.

(48) Watts, M. C.; Picco, L.; Russell-Pavier, F. S.; Cullen, P. L.; Miller, T. S.; Bartuś, S. P.; Payton, O. D.; Skipper, N. T.; Tileli, V.; Howard, C. A. Production of Phosphorene Nanoribbons. *Nature* **2019**, *568* (7751), 216–220. https://doi.org/10.1038/s41586-019-1074-x.
(49) Zhang, H.; Hu, W.; Du, A.; Lu, X.; Zhang, Y.; Zhou, J.; Lin, X.; Tang, Y. Doped Phosphorene for Hydrogen Capture: A DFT Study. *Applied Surface Science* **2018**, *433*, 249–255. https://doi.org/10.1016/j.apsusc.2017.09.243.
(50) Sibari, A.; Kerrami, Z.; Kara, A.; Hamedoun, M.; Benyoussef, A.; Mounkachi, O.; Benaissa, M. Adsorption and Diffusion on a Phosphorene Monolayer: A DFT Study. *J Solid State Electrochem* **2018**, *22* (1), 11–16. https://doi.org/10.1007/s10008-017-3703-3.
(51) Cortés-Arriagada, D. Phosphorene as a Template Material for Physisorption of DNA/RNA Nucleobases and Resembling of Base Pairs: A Cluster DFT Study and Comparisons with Graphene. *J. Phys. Chem. C* **2018**, *122* (9), 4870–4880. https://doi.org/10.1021/acs.jpcc.7b11268.
(52) Rubio-Pereda, P.; H. Cocoletzi, G. Density Functional Theory Calculations of Biomolecules Adsorption on Phosphorene for Biomedical Applications. *Applied Surface Science* **2018**, *427*, 1227–1234. https://doi.org/10.1016/j.apsusc.2017.08.198.
(53) Allec, S. I.; Wong, B. M. Inconsistencies in the Electronic Properties of Phosphorene Nanotubes: New Insights from Large-Scale DFT Calculations. *J. Phys. Chem. Lett.* **2016**, *7* (21), 4340–4345. https://doi.org/10.1021/acs.jpclett.6b02271.
(54) Zhang, R.-Y.; Zheng, J.-M.; Jiang, Z.-Y. Strain Effects on Properties of Phosphorene and Phosphorene Nanoribbons: A DFT and Tight Binding Study. *Chinese Phys. Lett.* **2018**, *35* (1), 017302. https://doi.org/10.1088/0256-307X/35/1/017302.
(55) Soler, J. M.; Artacho, E.; Gale, J. D.; García, A.; Junquera, J.; Ordejón, P.; Sánchez-Portal, D. The SIESTA Method Forab Initioorder-Nmaterials Simulation. *J. Phys.: Condens. Matter* **2002**, *14* (11), 2745–2779. https://doi.org/10.1088/0953-8984/14/11/302.
(56) Zhao, Y.-P.; Ye, D.-X.; Wang, P.-I.; Wang, G.-C.; Lu, T.-M. FABRICATION OF Si NANOCOLUMNS AND Si SQUARE SPIRALS ON SELF-ASSEMBLED MONOLAYER COLLOID SUBSTRATES. *Int. J. Nanosci.* **2002**, *01* (01), 87–97. https://doi.org/10.1142/S0219581X02000073.
(57) Shen, Z.; Hu, Z.; Wang, W.; Lee, S.-F.; Li, Y.; Gu, T.; Yu, J. C. Crystalline Phosphorus Fibers: Controllable Synthesis and Visible-Light-Driven Photocatalytic Activity. **2012**, 5.
(58) Ziletti, A.; Carvalho, A.; Campbell, D. K.; Coker, D. F.; Castro Neto, A. H. Oxygen Defects in Phosphorene. *Phys. Rev. Lett.* **2015**, *114* (4), 046801. https://doi.org/10.1103/PhysRevLett.114.046801.
(59) Akhtar, M.; Anderson, G.; Zhao, R.; Alruqi, A.; Mroczkowska, J. E.; Sumanasekera, G.; Jasinski, J. B. Recent Advances in Synthesis, Properties, and Applications of Phosphorene. *npj 2D Materials and Applications* **2017**, *1* (1), 1–13. https://doi.org/10.1038/s41699-017-0007-5.
(60) Liu, H.; Neal, A. T.; Zhu, Z.; Luo, Z.; Xu, X.; Tománek, D.; Ye, P. D. Phosphorene: An Unexplored 2D Semiconductor with a High Hole Mobility. *ACS Nano* **2014**, *8* (4), 4033–4041. https://doi.org/10.1021/nn501226z.
(61) Liu, H.; Lian, P.; Zhang, Q.; Yang, Y.; Mei, Y. The Preparation of Holey Phosphorene by Electrochemical Assistance. *Electrochemistry Communications* **2019**, *98*, 124–128. https://doi.org/10.1016/j.elecom.2018.12.007.
(62) Hanlon, D.; Backes, C.; Doherty, E.; Cucinotta, C. S.; Berner, N. C.; Boland, C.; Lee, K.; Harvey, A.; Lynch, P.; Gholamvand, Z.; Zhang, S.; Wang, K.; Moynihan, G.; Pokle, A.; Ramasse, Q. M.; McEvoy, N.; Blau, W. J.; Wang, J.; Abellan, G.; Hauke, F.; Hirsch, A.; Sanvito, S.; O'Regan, D. D.; Duesberg, G. S.; Nicolosi, V.; Coleman, J. N. Liquid Exfoliation of Solvent-Stabilized Few-Layer Black Phosphorus for Applications beyond Electronics. *Nat Commun* **2015**, *6* (1), 8563. https://doi.org/10.1038/ncomms9563.

(63) Dinh, K. N.; Zhang, Y.; Sun, W. The Synthesis of Black Phosphorus: From Zero- to Three-Dimensional Nanostructures. *J. Phys. Energy* **2021**, *3* (3), 032007. https://doi.org/10.1088/2515-7655/abf2da.
(64) Kumar, A. Controlled Nanostructures and Simultaneous Passivation of Black Phosphorus (Phosphorene) with Nafion. *Journal of Materials Research* **2020**, *35* (2), 141–152. https://doi.org/10.1557/jmr.2019.395.
(65) Guo, Z.; Zhang, H.; Lu, S.; Wang, Z.; Tang, S.; Shao, J.; Sun, Z.; Xie, H.; Wang, H.; Yu, X.-F.; Chu, P. K. From Black Phosphorus to Phosphorene: Basic Solvent Exfoliation, Evolution of Raman Scattering, and Applications to Ultrafast Photonics. *Advanced Functional Materials* **2015**, *25* (45), 6996–7002. https://doi.org/10.1002/adfm.201502902.
(66) van Setten, M. J.; Giantomassi, M.; Bousquet, E.; Verstraete, M. J.; Hamann, D. R.; Gonze, X.; Rignanese, G.-M. The PseudoDojo: Training and Grading a 85 Element Optimized Norm-Conserving Pseudopotential Table. *Computer Physics Communications* **2018**, *226*, 39–54. https://doi.org/10.1016/j.cpc.2018.01.012.
(67) Smidstrup, S.; Stradi, D.; Wellendorff, J.; Khomyakov, P. A.; Vej-Hansen, U. G.; Lee, M.-E.; Ghosh, T.; Jónsson, E.; Jónsson, H.; Stokbro, K. First-Principles Green's-Function Method for Surface Calculations: A Pseudopotential Localized Basis Set Approach. *Physical Review B* **2017**, *96* (19). https://doi.org/10.1103/PhysRevB.96.195309.
(68) Zhu, F.; Yin, H.; Wei, N.; Wan, J. Numerical Study of Thermal Conductivity Based on Phosphorene Anisotropy: Including [110] Direction and Related Phosphorus Nanotubes. *Materials Today Communications* **2020**, *22*, 100814. https://doi.org/10.1016/j.mtcomm.2019.100814.
(69) Wu, L.; Yang, W.; Wang, G. Mechanism of Substrate-Induced Anisotropic Growth of Monolayer WS 2 by Kinetic Monte Carlo Simulations. *npj 2D Materials and Applications* **2019**, *3* (1), 1–7. https://doi.org/10.1038/s41699-019-0088-4.
(70) Chen, Y.; Cui, P.; Ren, X.; Zhang, C.; Jin, C.; Zhang, Z.; Shih, C.-K. Fabrication of MoSe 2 Nanoribbons via an Unusual Morphological Phase Transition. *Nature Communications* **2017**, *8* (1), 15135. https://doi.org/10.1038/ncomms15135.
(71) Röder, H.; Hahn, E.; Brune, H.; Bucher, J.-P.; Kern, K. Building One- and Two-Dimensional Nanostructures by Diffusion-Controlled Aggregation at Surfaces. *Nature* **1993**, *366* (6451), 141–143. https://doi.org/10.1038/366141a0.
(72) Zhang, Z.; Chen, X.; Lagally, M. G. Bonding-Geometry Dependence of Fractal Growth on Metal Surfaces. *Phys. Rev. Lett.* **1994**, *73* (13), 1829–1832. https://doi.org/10.1103/PhysRevLett.73.1829.
(73) Zhang, J.; Fu, C.; Song, S.; Du, H.; Zhao, D.; Huang, H.; Zhang, L.; Guan, J.; Zhang, Y.; Zhao, X.; Ma, C.; Jia, C.-L.; Tománek, D. Changing the Phosphorus Allotrope from a Square Columnar Structure to a Planar Zigzag Nanoribbon by Increasing the Diameter of Carbon Nanotube Nanoreactors. *Nano Lett.* **2020**, *20* (2), 1280–1285. https://doi.org/10.1021/acs.nanolett.9b04741.
(74) Yu, Y.; Yao, J.; Niu, X.; Xing, B.; Liu, Y.; Wu, X.; Li, M.; Yan, X.; Sha, J.; Wang, Y. Synthesis and Electrical Properties of Single Crystalline Black Phosphorus Nanoribbons. *CrystEngComm* **2020**, *22* (22), 3824–3830. https://doi.org/10.1039/D0CE00390E.
(75) Liu, Z.; Sun, Y.; Cao, H.; Xie, D.; Li, W.; Wang, J.; Cheetham, A. K. Unzipping of Black Phosphorus to Form Zigzag-Phosphorene Nanobelts. *Nature Communications* **2020**, *11* (1), 3917. https://doi.org/10.1038/s41467-020-17622-6.
(76) Masih Das, P.; Danda, G.; Cupo, A.; Parkin, W. M.; Liang, L.; Kharche, N.; Ling, X.; Huang, S.; Dresselhaus, M. S.; Meunier, V.; Drndić, M. Controlled Sculpture of Black Phosphorus Nanoribbons. *ACS Nano* **2016**, *10* (6), 5687–5695. https://doi.org/10.1021/acsnano.6b02435.

(77) W, L.; Y, Y.; G, Z.; Yw, Z. Ultrafast and Directional Diffusion of Lithium in Phosphorene for High-Performance Lithium-Ion Battery. *Nano Lett* **2015**, *15* (3), 1691–1697. https://doi.org/10.1021/nl504336h.
(78) Güniat, L.; Caroff, P.; Fontcuberta i Morral, A. Vapor Phase Growth of Semiconductor Nanowires: Key Developments and Open Questions. *Chem. Rev.* **2019**, *119* (15), 8958–8971. https://doi.org/10.1021/acs.chemrev.8b00649.

Graphical abstract